The forward and inverse problem of cardiac magnetic fields based on concentric ellipsoid torso-heart model*

Wang Qian(王 倩)[a)b)], Hua Ning(华 宁)[a)], Tang Xue-Zheng(唐雪正)[a)], Lu Hong(陆 宏)[a)], Ma Ping(马 平)[b)†], and Tang Fa-Kuan(唐发宽)[a)‡]

[a)] *Department of Cardiology, the 309th Hospital of PLA, Beijing* 100091, *China*
[b)] *Department of Physics, State Key Laboratory for Artificial Microstructure and Mesoscopic Physics, Peking University, Beijing* 100871, *China*

(Received 24 August 2009; revised manuscript received 22 January 2010)

This paper constructs a concentric ellipsoid torso-heart model by boundary element method and investigates the impacts of model structures on the cardiac magnetic fields generated by both equivalent primary source—a current dipole and volume currents. Then by using the simulated magnetic fields based on the torso-heart model as input, the cardiac current sources—an array of current dipoles by optimal constrained linear inverse method are constructed. Next, the current dipole array reconstruction considering boundaries are compared with that in an unbounded homogeneous medium. Furthermore, the influence of random noise on reconstruction is also considered and the reconstructing effect is judged by several reconstructing parameters.

Keywords: concentric ellipsoid torso-heart model, boundary element method, current dipole array reconstruction, optimal constrained linear inverse method

PACC: 0650, 8740, 8770

1. Introduction

Human body is a complicate system, within which tissues and organs correlate with each other to play their roles in sustaining the significant metabolisms and physiological activities. In every part of the human body, there exist electrophysiological activities characterized by ionic motivations and excitation propagations, generating the electric potentials on the surface of each tissue and organ, and the magnetic fields outside the human torso. For researchers studying heart mechanisms, electric and magnetic signals from human heart are so valuable that they could offer specific information about cardiac activities. They can be recorded by electrocardiogram and magnetocardiogram (MCG),[1,2] providing doctors with powerful diagnostic criteria on heart-related diseases and being helpful in diagnosing those diseases in advance. The bio-magnetic fields caused by cardiac electrophysiological activities are the object of study in this paper.

The cardiac magnetic field detected outside the human torso results mainly from two sources: one is the bioelectric current—the real cardiac sources flowing within cardiac muscles; the other is the so-called volume currents generated by bioelectric currents and flowing passively throughout the body to complete the 'circuit'.[3] If the characteristics of cardiac electrophysiological activities are to be studied, the impact of volume currents, closely related to the tissue or organ structures, should be evaluated together. Along with the fast development of numerical computation technology, various tessellating methods emerge, such as the boundary element method (BEM) and the finite element method, which solve the forward problems of constructing irregularly shaped volume conductor models,[4,5] and simulate electric potentials and magnetic fields based on varied conductors.

After having mathematical models, researchers adopt them to deal with inverse problems, such as the electric and magnetic imaging—equivalent source reconstructions, under most conditions. The equivalent source could be one or more current dipoles or current multipole with undefined positions, magnitudes and orientations. To find the unknown parameters

*Project supported by the State Key Development Program for Basic Research of China (Grant No. 2006CB601007), the National Natural Science Foundation of China (Grant No. 10674006) and the National High Technology Research and Development Program of China (Grant No. 2007AA03Z238).
†Corresponding author. E-mail: maping@pku.edu.cn
‡E-mail: tfk616@yahoo.com.cn
© 2010 Chinese Physical Society and IOP Publishing Ltd

by a least fit, the iterative solution is required which leads to expensive computations.[6−12] Another kind of equivalent source is an array of current dipoles with fixed positions but unknown magnitudes and orientations, which can be calculated by solving matrix-equation directly without iteration.[13−15] The current dipole array is the source model to be reconstructed in this paper.

This paper mainly discusses the forward problem and the inverse problem of cardiac magnetic fields. In the forward problem, on account of the method put forward by Barr *et al.*[16] and the improved BEM,[17,18] a concentric ellipsoid model is constructed, and how the torso structures have effects on the external magnetic field excited by cardiac sources is investigated. When it comes to the inverse problem, the cardiac current source imaging is realized by optimally constrained linear inverse method (OCLIM).[13] Moreover, the influence of noise with diverse signal-to-noise ratios (SNRs) on imaging is studied and several reconstruction parameters are put forward.

2. Methods

2.1. Forward problem

Inside the human heart, the total current density $\boldsymbol{J}$ can be divided into two parts: the bioelectric current density $\boldsymbol{J}^i$ and the volume current density $\boldsymbol{J}^v$ responding passively to $\boldsymbol{J}^i$, i.e.

$$\boldsymbol{J} = \boldsymbol{J}^i + \boldsymbol{J}^v = \boldsymbol{J}^i - \sigma\boldsymbol{\nabla}V. \tag{1}$$

The human torso, deemed as a bounded piecewise conductor G with $\sigma = 0$ outside it, can be divided by diverse inner tissue surfaces S_j, $j = 1, 2\ldots, m$, into sub-regions G_j, $j = 1, 2\ldots, m$, whose conductivity σ_j is constant, so the electric potentials on surface S_k and the magnetic fields outside G can be expressed as[19]

$$\begin{aligned} V(\boldsymbol{r}) =\ & \frac{2\sigma_0}{(\sigma'_k+\sigma''_k)}V_0(\boldsymbol{r}) \\ & - \frac{1}{2\pi}\sum_{j=1}^{m}\frac{(\sigma'_j-\sigma''_j)}{(\sigma'_k+\sigma''_k)} \\ & \times \int_{S_j} V(\boldsymbol{r}')\boldsymbol{\nabla}'\frac{1}{|\boldsymbol{r}-\boldsymbol{r}'|}\cdot\boldsymbol{n}_j\mathrm{d}S_j, \end{aligned} \tag{2}$$

$$\begin{aligned} \boldsymbol{B}(\boldsymbol{r}) =\ & \boldsymbol{B}_0(\boldsymbol{r}) + \frac{\mu_0}{4\pi}\sum_{j=1}^{m}(\sigma'_j-\sigma''_j) \\ & \times \int_{S_j} V(\boldsymbol{r}')\boldsymbol{\nabla}'\frac{1}{|\boldsymbol{r}-\boldsymbol{r}'|}\times\boldsymbol{n}_j\mathrm{d}S_j, \end{aligned} \tag{3}$$

where

$$V_0(\boldsymbol{r}) = \frac{1}{4\pi\sigma_0}\int_G \boldsymbol{J}^i(\boldsymbol{r}')\cdot\boldsymbol{\nabla}'\frac{1}{|\boldsymbol{r}-\boldsymbol{r}'|}\mathrm{d}^3r', \tag{4}$$

$$\boldsymbol{B}_0(\boldsymbol{r}) = \frac{\mu_0}{4\pi}\int_G \boldsymbol{J}^i(\boldsymbol{r}')\times\boldsymbol{\nabla}'\frac{1}{|\boldsymbol{r}-\boldsymbol{r}'|}\mathrm{d}^3r', \tag{5}$$

$(\sigma'_j-\sigma''_j)V(\boldsymbol{r}')\boldsymbol{n}_j$ is equivalent to the surface current density due to the sudden change of conductivity on the interface S_j, $\boldsymbol{n}_j$ is the unit vector pointing to the outside of $\mathrm{d}S_j$, σ'_j and σ''_j are the conductivities on the inner and outer sides of S_j, σ_0 is the conductivity in area containing current sources.

In order to calculate the $V(\boldsymbol{r})$ and $\boldsymbol{B}(\boldsymbol{r})$ numerically, the second integral terms on the right-hand side of Eqs. (2) and (3) should be discrete. According to the concentric ellipsoid model constructed in this paper (as shown in Fig. 1), the human heart with surface S_H is supposed to be homogenous with conductivity σ_1, so is the area between S_H and torso surface S_B, with conductivity σ_2. In this case, equations (2) and (3) can be rewritten as

$$V_\mathrm{B}(\boldsymbol{r}) = \frac{2\sigma_0}{\sigma_2}V_{0\mathrm{B}}(\boldsymbol{r}) + \frac{1}{2\pi}\frac{\sigma_1-\sigma_2}{\sigma_2}\int_{S_\mathrm{H}} V_\mathrm{H}(\boldsymbol{r}')\mathrm{d}\Omega^{\boldsymbol{r}}_{\mathrm{BH}}(\boldsymbol{r}') + \frac{1}{2\pi}\int_{S_\mathrm{B}} V_\mathrm{B}(\boldsymbol{r}')\mathrm{d}\Omega^{\boldsymbol{r}}_{\mathrm{BB}}(\boldsymbol{r}'), \tag{6}$$

$$V_\mathrm{H}(\boldsymbol{r}) = \frac{2\sigma_0}{\sigma_1+\sigma_2}V_{0\mathrm{H}}(\boldsymbol{r}) + \frac{1}{2\pi}\frac{\sigma_1-\sigma_2}{\sigma_1+\sigma_2}\int_{S_\mathrm{H}} V_\mathrm{H}(\boldsymbol{r}')\mathrm{d}\Omega^{\boldsymbol{r}}_{\mathrm{HH}}(\boldsymbol{r}') + \frac{1}{2\pi}\frac{\sigma_2}{\sigma_1+\sigma_2}\int_{S_\mathrm{B}} V_\mathrm{B}(\boldsymbol{r}')\mathrm{d}\Omega^{\boldsymbol{r}}_{\mathrm{HB}}(\boldsymbol{r}'), \tag{7}$$

$$\boldsymbol{B}(\boldsymbol{r}) = \boldsymbol{B}_0(\boldsymbol{r}) + \frac{\mu_0}{4\pi}(\sigma_1-\sigma_2)\int_{S_\mathrm{H}} V_\mathrm{H}(\boldsymbol{r}')\boldsymbol{\nabla}'\frac{1}{|\boldsymbol{r}-\boldsymbol{r}'|}\times\boldsymbol{n}_\mathrm{H}\mathrm{d}S_\mathrm{H} + \frac{\mu_0}{4\pi}\sigma_2\int_{S_\mathrm{B}} V_\mathrm{B}(\boldsymbol{r}')\boldsymbol{\nabla}'\frac{1}{|\boldsymbol{r}-\boldsymbol{r}'|}\times\boldsymbol{n}_\mathrm{B}\mathrm{d}S_\mathrm{B}. \tag{8}$$

Using the node-to-node discrete pattern on the surface of concentric ellipsoid, we tessellate the surface S_B and S_H into many small triangles according to Barr's method (1977) and express Eqs. (6) and (7) in a matrix form:

$$\begin{pmatrix} P_{\mathrm{BB}} & P_{\mathrm{BH}} \\ P_{\mathrm{HB}} & P_{\mathrm{HH}} \end{pmatrix}\begin{pmatrix} V_\mathrm{B} \\ V_\mathrm{H} \end{pmatrix} = -\begin{pmatrix} \dfrac{2\sigma_1}{\sigma_2}V_{0\mathrm{B}} \\ \dfrac{2\sigma_1}{\sigma_1+\sigma_2}V_{0\mathrm{H}} \end{pmatrix}, \tag{9}$$

where, $V_{\rm B} = (V_{\rm B}^1, V_{\rm B}^2, \ldots, V_{\rm B}^{I_{\rm B}})^{\rm T}$, $V_{\rm H} = (V_{\rm H}^1, V_{\rm H}^2, \ldots, V_{\rm H}^{I_{\rm H}})^{\rm T}$ are potential vectors containing potentials on $I_{\rm B}$ and $I_{\rm H}$ located on surfaces $S_{\rm B}$ and $S_{\rm H}$. Matrix $P = \begin{pmatrix} P_{\rm BB} & P_{\rm BH} \\ P_{\rm HB} & P_{\rm HH} \end{pmatrix}$ is only related to the geometrical characteristics of surface $S_{\rm B}$ and $S_{\rm H}$.

From Eq. (4) and the constructed model, the magnetic field at $\boldsymbol{r}_i$ normal to the observation plane ($\boldsymbol{e}_i$ is the unit outer normal vector) is

$$\begin{aligned} B_i(\boldsymbol{r}) = {} & B_{0i}(\boldsymbol{r}) + \frac{\mu_0}{4\pi}(\sigma_1 - \sigma_2) \sum_{j=1}^{K_{\rm H}} \Phi_{\rm H}^j \frac{\boldsymbol{r}_i - \boldsymbol{r}_{\rm H}^{j\,\prime}}{\left|\boldsymbol{r}_i - \boldsymbol{r}_{\rm H}^{j\,\prime}\right|^3} \\ & \times \boldsymbol{n}_{\rm H}^j \cdot \boldsymbol{e}_i \Delta S_{\rm H}^j + \frac{\mu_0}{4\pi}\sigma_2 \sum_{j=1}^{K_{\rm B}} \Phi_{\rm B}^j \frac{\boldsymbol{r}_i - \boldsymbol{r}_{\rm B}^{j\,\prime}}{\left|\boldsymbol{r}_i - \boldsymbol{r}_{\rm H}^{j\,\prime}\right|^3} \\ & \times \boldsymbol{n}_{\rm B}^j \cdot \boldsymbol{e}_i \Delta S_{\rm B}^j, \end{aligned} \tag{10}$$

where, $K_{\rm B}$ and $K_{\rm H}$ are triangle numbers on surfaces $S_{\rm B}$ and $S_{\rm H}$, $\Phi_{\rm B}^j$ and $\Phi_{\rm H}^j$ are chosen to be the mean potential of the three apex-potentials of the triangles $\Delta S_{\rm B}^j$ and $\Delta S_{\rm H}^j$, $\Phi_{\rm B} = (\Phi_{\rm B}^1, \Phi_{\rm B}^2, \ldots, \Phi_{\rm B}^{K_{\rm B}})^{\rm T}$, $\Phi_{\rm H} = (\Phi_{\rm H}^1, \Phi_{\rm H}^2, \ldots, \Phi_{\rm H}^{K_{\rm H}})^{\rm T}$. The relationship between $V_{\rm B}$ and $\Phi_{\rm B}$, $V_{\rm H}$ and $\Phi_{\rm H}$ can be expressed by $\Phi_{\rm B} = \frac{1}{3} D_{\rm B}^{\rm T} V_{\rm B}$, $\Phi_{\rm H} = \frac{1}{3} D_{\rm H}^{\rm T} V_{\rm H}$, the elements of each row vector of the matrix D (dimension of $I_{\rm B} \times K_{\rm B}$ or $I_{\rm H} \times K_{\rm H}$) are defined as: as to one node, any triangle employing this node to be its apex will make the corresponding element of D unit, otherwise zero.

In Section 3, we will discuss the magnetic field distribution on the observation plane calculated by BEM, and its variation with the change of torso-heart model structures.

2.2. Inverse problem

2.2.1. Lead field

According to the discussions in the above section, the magnetic field on observation point $\boldsymbol{r}_i$ and the corresponding equation for electric potential at point $\boldsymbol{r}_k$ on torso surface can be written in a matrix form:[20]

$$B_i = B_{0,i} + \sum_{m=1}^{K_{\rm B}} A_{im}^{\rm B} V_{0,m}^{\rm B} + \sum_{n=1}^{K_{\rm H}} A_{in}^{\rm H} V_{0,n}^{\rm H}, \tag{11}$$

$$V_k = \sum_{m=1}^{K_{\rm B}} C_{km}^{\rm B} V_{0,m}^{\rm B} + \sum_{n=1}^{K_{\rm H}} C_{kn}^{\rm H} V_{0,n}^{\rm H}. \tag{12}$$

As to B_i and V_k, they have linear relationship with the primary current density as stated by Hamalainen and Ilmoniemi:[21]

$$B_i = \int_G L_i(\boldsymbol{r}') \cdot \boldsymbol{J}^i(\boldsymbol{r}') {\rm d}^3 r', \tag{13}$$

$$V_k = \int_G \boldsymbol{L}_k^{\boldsymbol{E}}(\boldsymbol{r}') \cdot \boldsymbol{J}^i(\boldsymbol{r}') {\rm d}^3 r', \tag{14}$$

where, $\boldsymbol{L}_i$ and $\boldsymbol{L}_k^{\boldsymbol{E}}$ are lead field of a magnetometer at $\boldsymbol{r}_i$ and electric lead field of an electrode at $\boldsymbol{r}_k$. They are concerned with source, observation point distributions and model geometries:

$$\begin{aligned} \boldsymbol{L}_i(\boldsymbol{r}') = {} & \boldsymbol{L}_{0,i}(\boldsymbol{r}') + \sum_{m=1}^{K_{\rm B}} A_{im}^{\rm B} \boldsymbol{L}_{0,m}^{\boldsymbol{E}}(\boldsymbol{r}') \\ & + \sum_{n=1}^{K_{\rm H}} A_{in}^{\rm H} \boldsymbol{L}_{0,n}^{\boldsymbol{E}}(\boldsymbol{r}'), \end{aligned} \tag{15}$$

$$\begin{aligned} \boldsymbol{L}_k^{\boldsymbol{E}}(\boldsymbol{r}') = {} & \boldsymbol{L}_{0,k}^{\boldsymbol{E}}(\boldsymbol{r}') + \sum_{m=1}^{K_{\rm B}} C_{im}^{\rm B} \boldsymbol{L}_{0,m}^{\boldsymbol{E}}(\boldsymbol{r}') \\ & + \sum_{n=1}^{K_{\rm H}} C_{in}^{\rm H} \boldsymbol{L}_{0,n}^{\boldsymbol{E}}(\boldsymbol{r}'), \end{aligned} \tag{16}$$

where

$$\boldsymbol{L}_{0,i}(\boldsymbol{r}') = \frac{\mu_0}{4\pi} \frac{(\boldsymbol{r}_i - \boldsymbol{r}') \times \boldsymbol{e}_i}{|\boldsymbol{r}_i - \boldsymbol{r}'|^3},$$

$$\boldsymbol{L}_{0,k}^{\boldsymbol{E}}(\boldsymbol{r}') = \frac{1}{4\pi\sigma} \frac{\boldsymbol{r}_k - \boldsymbol{r}'}{|\boldsymbol{r}_k - \boldsymbol{r}'|^3}.$$

For simplification, the primary currents are supposed to be distributed on a thin layer with thickness h, which is parallel to the magnetic observation plane, and tessellated into N cells. Thus, equations (13) and (14) could be tessellated and rewritten in the form of summation:

$$B_i = \sum_{j=1}^{N} \boldsymbol{L}_i(\boldsymbol{r}_j') \cdot \boldsymbol{J}(\boldsymbol{r}_j') h \Delta S_j', \quad i = 1, 2, \ldots, m_{\rm B}, \tag{17}$$

$$V_k = \sum_{j=1}^{N} \boldsymbol{L}_k^{\boldsymbol{E}}(\boldsymbol{r}_j') \cdot \boldsymbol{J}(\boldsymbol{r}_j') h \Delta S_j', \quad k = 1, 2, \ldots, m_V, \tag{18}$$

where $\boldsymbol{J}(\boldsymbol{r}_j') h \Delta S_j'$ with dimension of A · m could be deemed as a current dipole $\boldsymbol{Q}_j$. In each cell of the thin layer, there will be a current dipole, composing the current dipole array, and this current dipole array will be deemed as the equivalent current sources.

As to all the measuring points of electric potential ($m_{\rm B}$ points in all) and magnetic field (m_V points in all), we have

$$b = Lq, \quad v = L^{\rm E} q, \tag{19}$$

where $b = (B_1, B_2, \ldots, B_{m_{\rm B}})^{\rm T}$, $v = (V_1, V_2, \ldots, V_{m_V})^{\rm T}$, $q = (\boldsymbol{Q}_1, \boldsymbol{Q}_2, \ldots, \boldsymbol{Q}_{\rm N})^{\rm T}$ are the collections of

all the measured magnetic field, measured electric potential and current dipoles, respectively, L and L^{E} are the matrices composed of all the lead fields and electric lead fields.

2.2.2. Inverse algorithm

On account of research interests of our research team, this paper plans to discuss the inverse computation of cardiac magnetic fields only.

In order to obtain the current dipole array, solving the ill-posed problem for the inverse of matrix L is the key point. In most cases, the essence of various inverse algorithms is to find the most optimally approximate solution $\hat{q}$, which minimizes the residual $\Delta^2 = \|b - L\hat{q}\|^2$ (guaranteeing the presence of the solution) and norm $\|\hat{q}\|^2$ (guaranteeing the uniqueness of the solution).

Furthermore, if the measurements are contaminated by some noise w, the measured magnetic fields can be written as:

$$b = Lq + w, \tag{20}$$

where, the noise vector w is assumed to be a random vector with mean zero.

In recent decades, there are many applicable methods put forward for resolving the inverse problem described above, for example, the most original and classic—minimum-norm least squares method, the optimal weighted pseudo-inverse method and its special case—the optimal truncated pseudo-inverse method, L-curve method[22] and the truncated total least square method.[23] In this paper, the optimal constrained linear inverse method[13] is chosen to solve the inverse problem, i.e. to find the best estimate $\hat{q}$ satisfying the matrix equation:

$$\hat{q} = Hb, \tag{21}$$

where H is the OCLIM estimator for source reconstruction,

$$H = (AL^{\mathrm{T}} + \Gamma)(LAL^{\mathrm{T}} + L\Gamma + \Gamma^{\mathrm{T}}L^{\mathrm{T}} + \Sigma)^{-1}, \tag{22}$$

in which the covariance matrix $A = Eqq^{\mathrm{T}}$, $\Sigma = Eww^{\mathrm{T}}$, the cross-covariance between the source and noise amplitude vectors is $\Gamma = Eqw^{\mathrm{T}}$.

3. Model construction

Figure 1 shows that the torso-heart concentric ellipsoid model is constructed. The human heart is supposed to be a sphere and the conductivities of the heart muscle and inner torso tissue is 0.10 S/m and 0.04 S/m, respectively.[18] The 6×6 mesh grid parallel to the XOY plane and 2 cm in front of the torso composes the observation plane, on which the external magnetic fields are detected at each node and the distance between two nearest nodes is 4 cm.

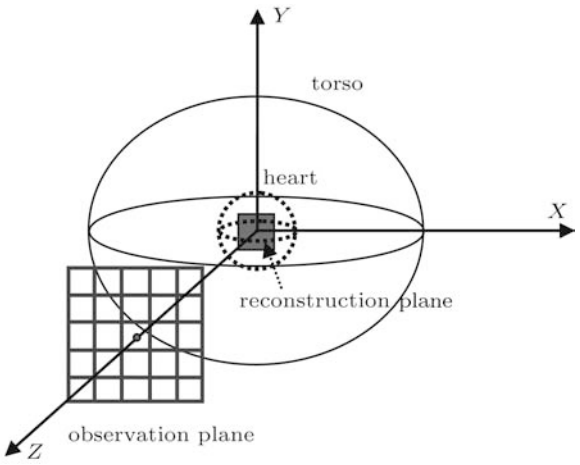


Fig. 1. The concentric ellipsoid model of human heart and torso, the magnetic observation plane and the reconstruction plane.

According to BEM, the heart and torso is tessellated node-to-node into a large amount of triangles and the specific tessellating pattern is given in Fig. 2. One of the small triangles is marked by red patch. From this pattern, 24 areas distribute evenly along the latitude and longitude, respectively, thus there appear 554 nodes and 1104 triangles on the surface of the heart and torso. Three axes a, b, c of the ellipsoid $x^2/a^2 + y^2/b^2 + z^2/c^2 = 1$ are chosen according to body structures roughly.

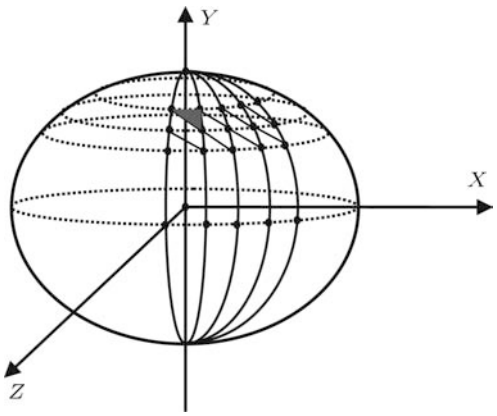


Fig. 2. The ellipsoid is tessellated into a large amount of triangles. A small triangle is marked by red patch.

In Section 4, we will consider the impact of the body shape on the magnetic field in front of human

torso and discuss modifications brought by surface currents to the MCG map.

After obtaining the cardiac magnetic fields, we will use them as the prior information for current dipole array imaging. The reconstruction plane (imaging plane), red square marked in Fig. 1, consists of rectangular grid-arranged current dipoles with fixed positions, while unfixed magnitudes and directions. The nearest distance between two dipoles is 0.5 mm. In Section 5, the result of dipole array imaging by OCLIM will be given, and the images based on the torso-heart model and in infinite medium will be compared. Furthermore, the influence from the random noise on the imaging effects will be considered in that section.

4. Results of the forward problem

The magnetic contributions due to surface currents on the interfaces separating two kinds of tissues are unavoidable for research when the cardiac magnetic field generated by the bioelectric sources is investigated. In this paper, a current dipole at the centre of the concentric ellipsoids is chosen as the functional source, a simple but proper cardiac approximation during the QRS complex and ST-T complex in one cardiac cycle. When torso structural parameters are chosen as follows: $a = 0.2$ m, $b = 0.2$ m, $c = 0.1$ m, and the heart model is a sphere with radius $r = 0.05$ m, the magnetic field B_0 resulting from the current dipole model without boundary modifications on the observation plane is given in Fig. 3.

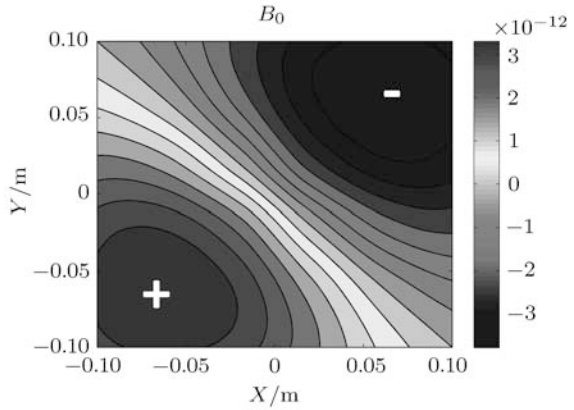


Fig. 3. The magnetic field B_0 resulting from the current dipole model without the boundary modifications on the observation plane. The sign '+' denotes the positive magnetic area and the sign '–' denotes the negative magnetic area.

Compared with the pure current dipole magnetic field B_0, the magnetic field B considering the influence of boundaries is shown in Fig. 4, where the contour of the modified B is roughly the same with that of B_0, but when it comes to details, the curvature of contour lines in both positive and negative areas of modified B is bigger than that of B_0, and the linear distance between the positive and the negative areas of modified B becomes about 0.1 m closer. From the colour bar, the magnitudes of B_0 are counteracted by the magnetic fields caused by surface currents on the interface, thus the magnitudes of B seem to be about one third of its original magnitudes.

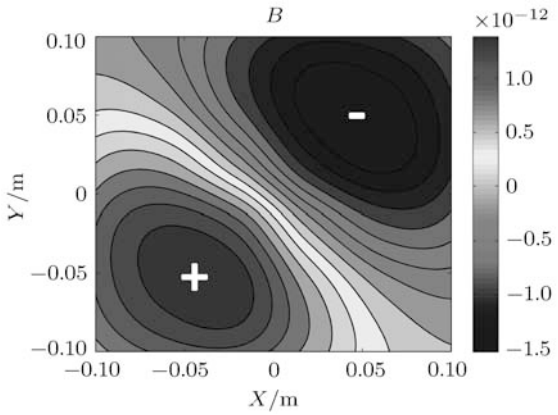


Fig. 4. The magnetic field B considering the influence of boundaries. The sign '+' denotes the positive magnetic area and '–' denotes the negative magnetic area.

4.1. The influence of torso width on the external magnetic field

This subsection discusses the influence of torso size, especially the width of the torso described by parameter a. The elliptic eccentricity $e = \sqrt{a^2 - c^2}/a$ is constant: $e = 0.85$, and a is chosen from 0.125 m to 0.30 m, $b = 0.2$ m. In addition, the cardiac is still treated as a sphere with radius $r = 0.05$ m. Thus the simulated results are given in Fig. 5.

From pictures from (a) to (h) in Fig. 5, we could find that when $a = 0.15$ m, 0.175 m, 0.2 m, 0.225 m, the surface currents have few impact on the structure of magnetic field B_0, even though the shape of the magnetic field has a little distortion. While when $a = 0.125$ m, 0.25 m, 0.275 m, 0.3 m, the structural distortion becomes bigger and the line linking the maximum and minimum values happens to rotate. If the torso width is too big or too small, the modifications from surface currents tend to be more significant. In the section of inverse problem the torso with $a = 0.2$ m will be chosen.

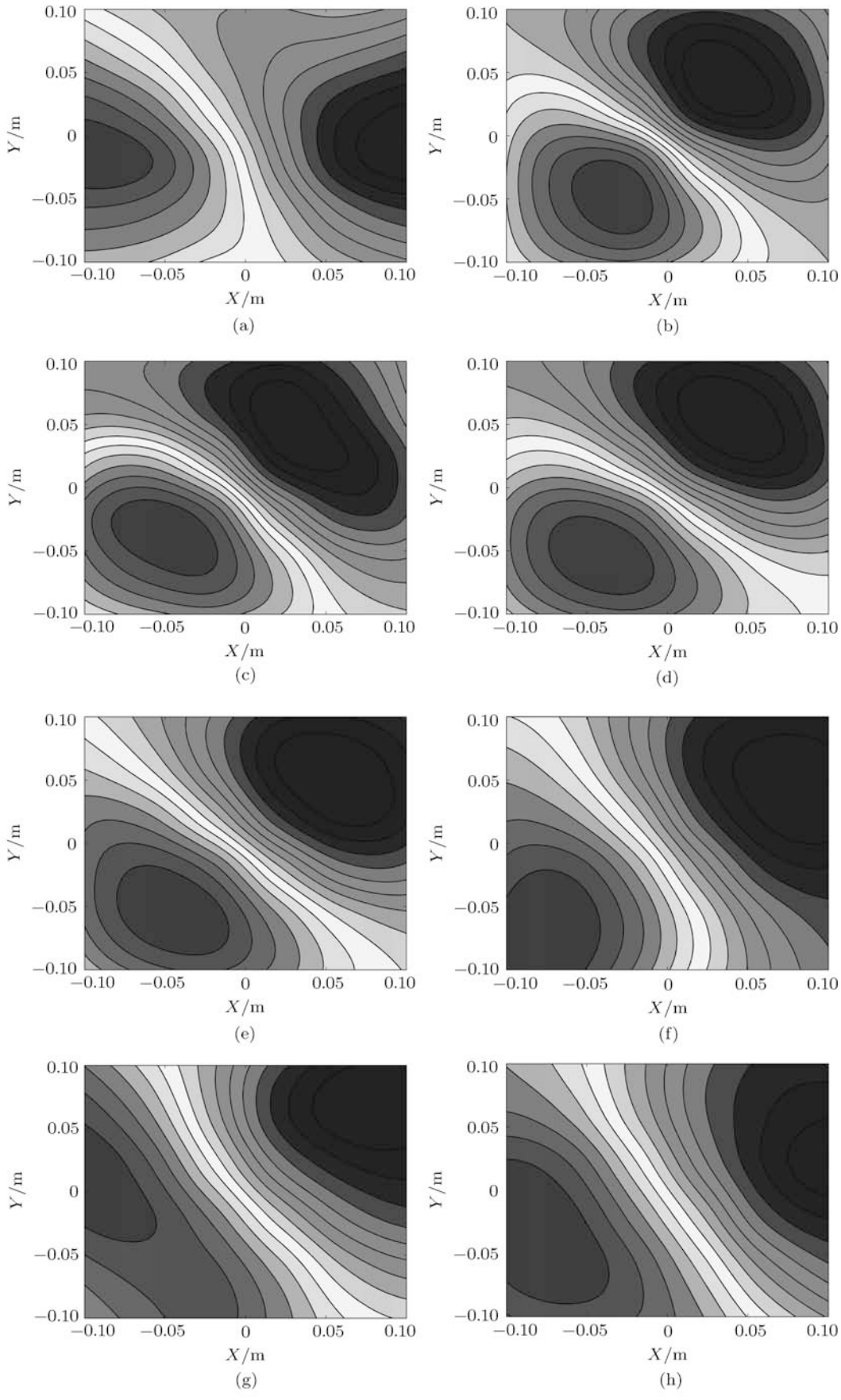


Fig. 5. The comparing charts of magnetic field B with different torso width $2a$. Pictures (a) to (h) have $a = 0.125$ m, 0.15 m, 0.175 m, 0.2 m, 0.225 m, 0.25 m, 0.275 m, and 0.3 m, respectively.

4.2. The influence of elliptic eccentricity on the external magnetic field

Here, the influence of the torso thickness $2c$ on the external magnetic field is studied. The elliptic eccentricity e is not constant any more, changing from 0.7 to 0.95 corresponding to c changing from 0.143 m to 0.062 m, $a = b = 0.2$ m. The comparing charts are obtained in Fig. 6.

From pictures (a) to (f) in Fig. 6, when the elliptic eccentricity is bigger, such as $e = 0.85$, 0.9, 0.95, the structures of magnetic field have little aberration from that of magnetic field B_0, while when the elliptic eccentricity is smaller, such as $e = 0.7$, 0.75, 0.8, contributions from the surface currents are more important, leading to greater distortion of the magnetic field. At the same time, the less the elliptic eccentricity is, the greater the distortion is.

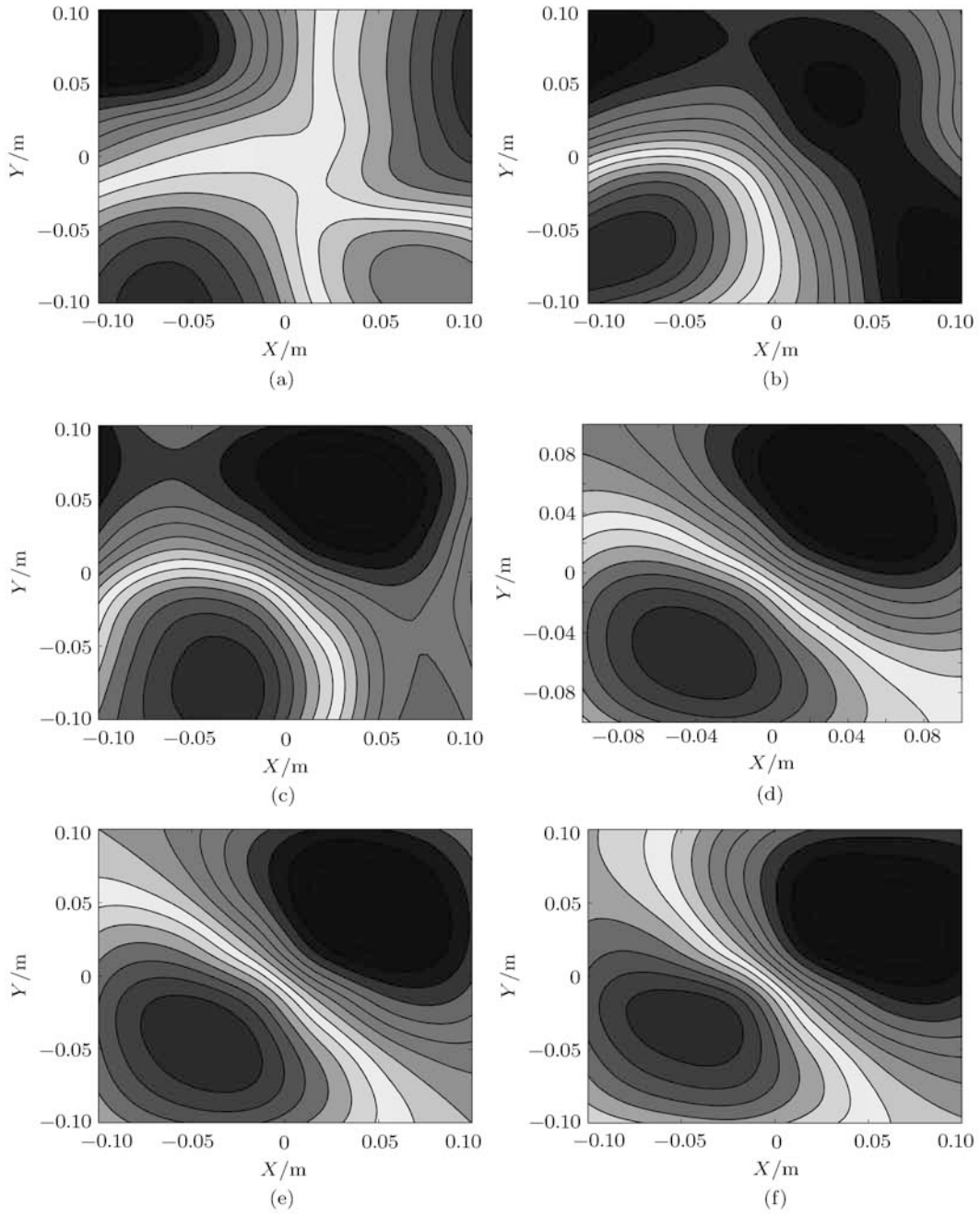


Fig. 6. The comparing charts of magnetic field B influenced by torso model with different elliptic eccentricity e. Pictures (a) to (f) have the elliptic eccentricity $e = 0.7$, 0.75, 0.8, 0.85, 0.9, 0.95, respectively.

According to Subsections 4.1 and 4.2, the external magnetic field, especially the perpendicular component, may be significantly influenced by the torso shape and internal inhomogeneities, which is also revealed by some other studies.[24,25] Understanding the influence of model structures on the external magnetic field is helpful to choosing the appropriate parameters for inverse problem—cardiac current source imaging.

5. Results of the inverse problem

Next, the cardiac magnetic inverse problem will be discussed based on the model put forward in the above section. The torso shape parameters are set to be $a = b = 0.2$ m, $c = 0.1$ m, the heart is also supposed to be a sphere with the same size as before. The current dipoles serving as cardiac electric sources are assumed to distribute evenly on a thin layer at the centre of the heart, the nearest distance between the two would-be reconstructed dipoles is 0.5 cm, and there are 14×14 dipoles in all.

5.1. The current dipole array imaging without noise

For comparison, the current dipole array reconstruction in an unbounded homogeneous medium is given in Fig. 7 first. From Fig. 7(a) describing the distribution of the x and y component of dipoles, current dipoles reconstructed in array is distributed symmetrically about the test source—a current dipole. Figure 7(b) manifests the 3D distribution of current dipoles. For most dipoles, they do not have the z component and this phenomenon is reasonable because only the z component of the external magnetic fields is detected, which is only generated by the x and y components of current sources, so when the current sources are reconstructed, they should only embrace the x and y components. As to a few reconstructed dipoles with z component, on account of their quite small z-values, this should be attributed to the computation errors when the inverse matrix of the lead field is calculated.

Then using the OCLIM, we realized the imaging of the current dipole array based on the torso-heart model, as shown in Fig. 8. Correspondingly, figure 8(a) is the 2D reconstruction of current dipole array on the XOY plane, and the dipole arrangement is influenced by the model boundaries, which leads to the reduction of its distributing symmetry. At the same time, figure 8(b) clearly shows that most of the reconstructed dipoles have their z component, whose magnitudes are relatively big. The reason for the appearance of z component is closely related to boundaries, i.e. x, y and z components of current sources generate the surface currents simultaneously, so the perpendicular magnetic field caused by surface currents will embrace the contribution from the z component of current sources, thus the reconstructed dipoles should have z component if the inverse process uses the perpendicular magnetic field as input.

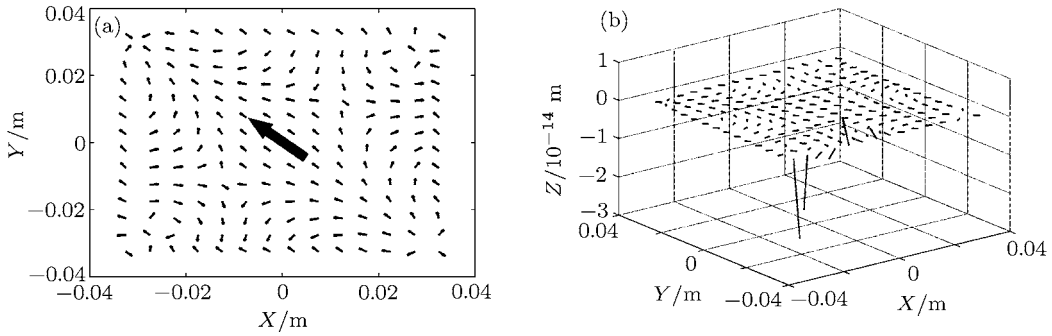


Fig. 7. The current dipole array reconstruction in an unbounded homogeneous medium. Picture (a) shows 2D reconstruction on XOY plane, the big arrow denotes the test source (a current dipole). Picture (b) shows 3D reconstruction.

In order to judge the quality of reconstruction, several parameters can be appealed. First, the reconstruction error $\eta^2 = E\,\|q - \hat{q}\|^2$, which is a measurement of the discrepancy between the reconstructed and the true current distributions. Second, the residual $\chi^2 = (b - F\hat{q})^{\mathrm{T}} E w w^{\mathrm{T}} (b - F\hat{q})$, which describes how closely the measured and the reconstructed field values match. Third, the mean value $E\chi^2$ of the residual reveals how closely a reconstruction matches the given measurements on average. But in reality, the OCLIM is more suitable

for the inverse computation with noise, so here for simulating the condition without noise, a random noise vector with extremely tiny magnitudes of each element (very high SNR) and mean zero is added. The current dipole array reconstruction in this paper has: $\eta^2 = 48.9927$, $E\chi^2 = 2.8968 \times 10^{-27}$, $\chi^2 = 3.3154 \times 10^4$ with SNR = 209.5434 dB.

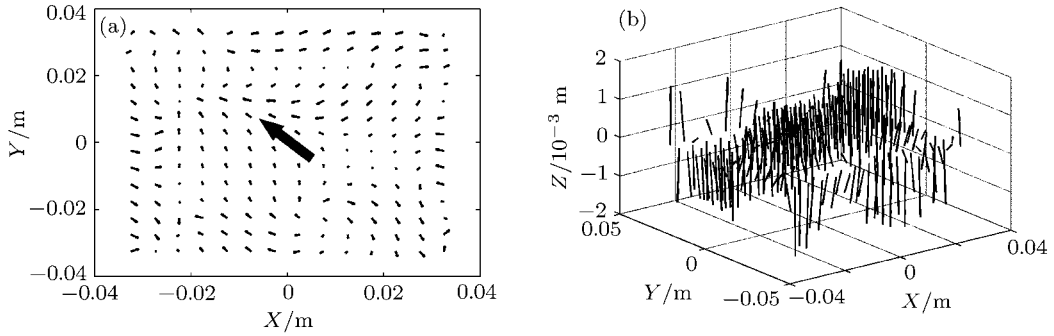
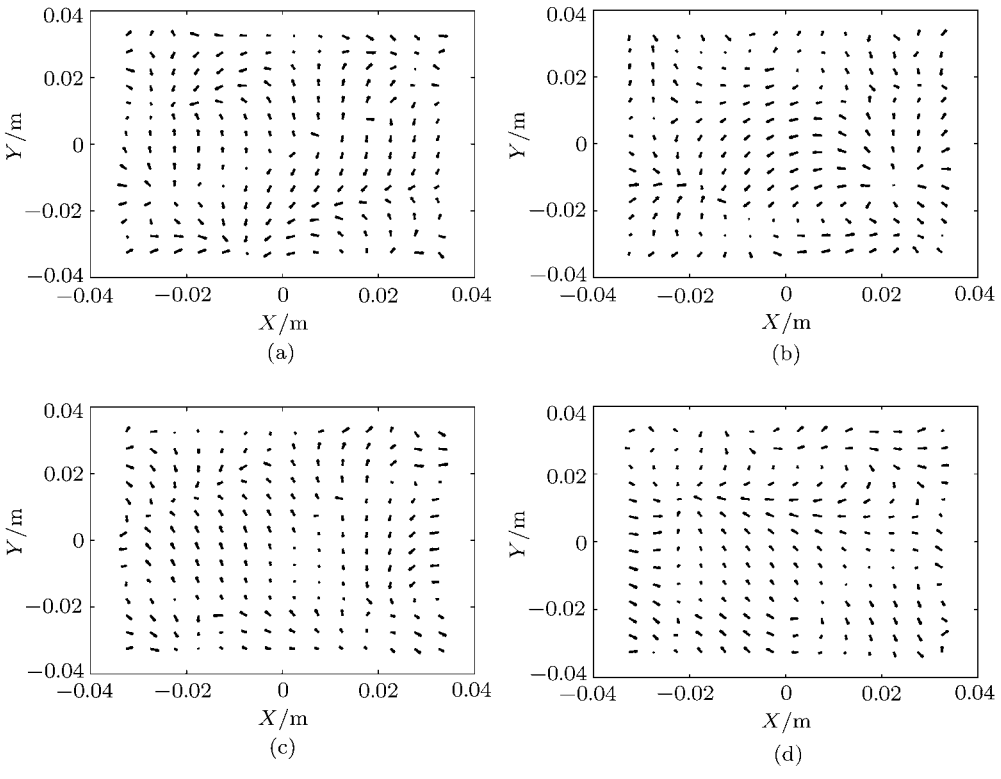


Fig. 8. The current dipole array reconstruction in the torso-heart model. Picture (a) shows the 2D reconstruction on XOY plane. Picture (b) shows the 3D reconstruction.

5.2. The current dipole array reconstruction with noise

In the process of measurement, various noises will appear, and here the most common kind of noise—random noise is simulated. We will mainly discuss the impact of the noise with diverse SNRs on reconstructing effects and the corresponding change of reconstruction parameters.

The basic structural properties are the same as before in this subsection, except that random noises are added to the equivalent measured magnetic field (simulated through forward problem). The current dipole array reconstructions under different SNRs are given in Fig. 9, where from pictures (a) to (f) the SNRs are −10.45663 dB, 15.8316 dB, 36.815 dB, 56.5983 dB, 76.1903 dB, and 96.6808 dB, respectively. When SNR is low, the asymmetry is obvious, while when SNR becomes higher, the dipoles are arranged more symmetrically, especially according to computation, if SNR is larger than 55 dB, the dipole arrangement is roughly the same as that under the condition when SNR is extremely large or there is no noise.



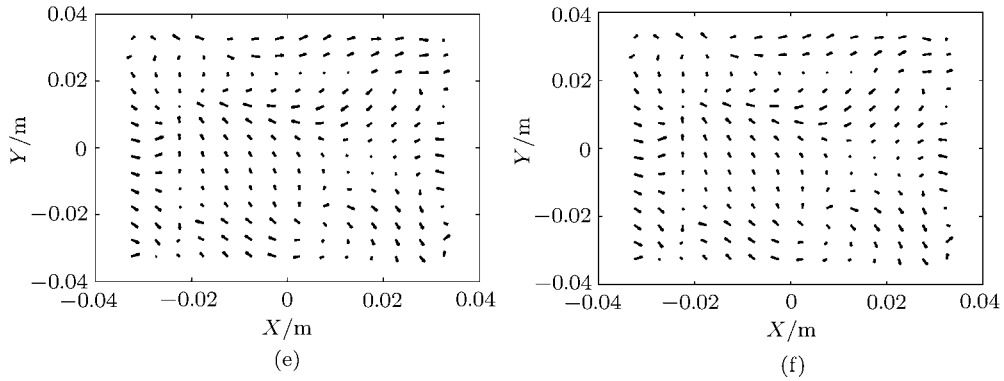


Fig. 9. Comparing charts of the current dipole array reconstruction with different noises. From picture (a) to (f), the SNRs are −10.45663 dB, 15.8316 dB, 36.815 dB, 56.5983 dB, 76.1903 dB, and 96.6808 dB, respectively.

As to the reconstruction parameters, η^2, χ^2 and $E\chi^2$, their trends with the change of SNR are given as follows. Figure 10 shows the reconstruction error η^2 as the function of SNR. It changes in a small scale from about 44 to 49 considering the different data points calculated in this paper. Figure 11 shows the residual χ^2 as the function of SNR (please note: y axis adopts χ^2's denary logarithm: $\log_{10}\chi^2$). It reaches the minimum at about 15 dB and at the two sides of this point, $\log_{10}\chi^2$ is monotonely increase or decreasing along with SNR's increasing. Figure 12 describes the mean residual $E\chi^2$ as the function of SNR. The $\log_{10} E\chi^2$ is linearly decreasing with the increasing of SNR.

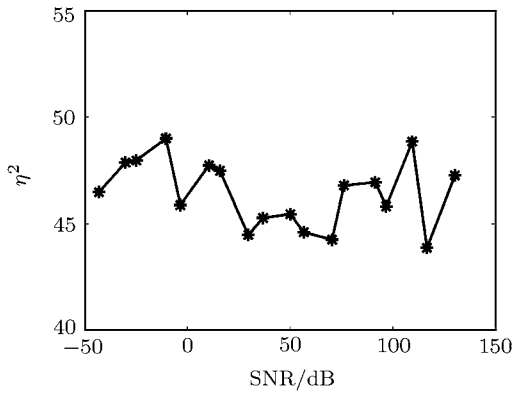


Fig. 10. Reconstruction error as the function of SNR.

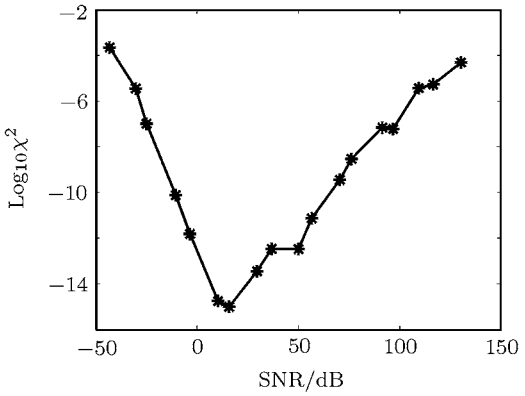


Fig. 11. Residual as the function of SNR. The $\log_{10}\chi^2$ serves as the scale of y axis.

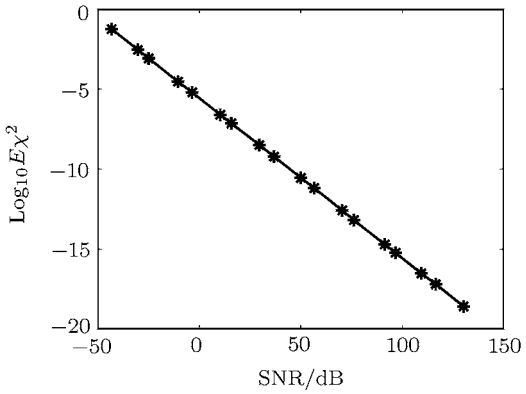


Fig. 12. Mean residual as the function of SNR. The $\log_{10} E\chi^2$ serves as the scale of y axis.

Only random noise is discussed in this paper, though there are other types of noise appearing in realistic measurements. The influences of other kinds of noise on the cardiac current source reconstruction will be studied in the next step and they will serve as an indispensible tool to decide what quality the signals should arrive at to meet the needs of imaging. Actually, the magnetic signals detected and processed by our MCG system already have SNR larger than 55 dB and they can basically satisfy the requirements for imaging and other computations related to cardiac magnetic fields.

6. Conclusion

In this paper, the influence from the surface currents on the external magnetic fields is considered based on a concentric ellipsoid torso-heart model constructed by BEM. The magnetic field B_0 in an unbounded medium is compared with the modified magnetic field B considering the boundary effect and we find, apart from the curvature of the magnetic contour lines and the distance between the positive and negative areas, their structures of magnetic field are roughly the same, but the magnitude of the magnetic field B is reduced to about one third of the original magnetic field B_0. Then, two structural factors impacting on the external magnetic distributions are investigated. One is the width of the human torso model and the other is the elliptic eccentricity of that model. As to the first factor, when the width is neither too big nor too small the boundary has less influence on the modified magnetic field B, in comparison with more extreme conditions where the modified magnetic field is distorted more intensively. As to the second factor, the structural distortions become less severe when the elliptic eccentricity gets bigger.

At the same time, the inverse problem is also discussed. Using the magnetic signals generated by a test source—a current dipole based on this torso-heart model, by OCLIM we reconstruct the cardiac current sources, assumed to be a current dipole array. When noises are set to be zero approximately, the dipoles in array are arranged symmetrically about the test source, while this symmetry is not as regular as that in an unbounded medium. If the random noises are added to the detected magnetic field, the reconstruction effect gets worse without any doubt. The dipoles are in disorder with low SNR, especially the negative SNR, but with the increase of SNR the reconstruction effects become well, in particular when SNR is larger than 55 dB. The current dipole array reconstruction with noise but SNR $>$ 55 dB is roughly the same as that without noise. Moreover, parameters representing the reconstructing qualities, such as reconstruction error η^2, residual χ^2 and mean residual $E\chi^2$, are calculated and their changes as the function of SNR are concluded. Studying the influence of noise on imaging plays the supervising role in determining what qualities the magnetic signals are needed for imaging.

References

[1] Ma P, Yao K, Xie F X, Zhang S Y, Deng P, He D F, Zhang F, Liu L Y, Nie R J, Wang F R, Wang S Z and Dai Y D 2002 *Acta Phys. Sin.* **51** 224 (in Chinese)

[2] Liu X Y, Xie F X, Meng S C, Ma P, Yang T, Nie R J, Wang S Z, Wang F R and Dai Y D 2003 *Acta Phys. Sin.* **52** 2580 (in Chinese)

[3] Jerbi K, Mosher J C, Baillet S and Leahy R M 2002 *Phys. Med. Biol.* **47** 523

[4] Nenonen J, Purcell C J, Horacek B M, Stroink G and Katila 1991 *IEEE Trans. Biomed. Eng.* **38** 658

[5] Wach P, Tilg B, Lafer G and Rucker W 1997 *Med. Biol. Comput.* **35** 157

[6] Arthur R M and Geselowitz D B 1970 *IEEE Trans. Biomed. Eng.* **17** 141

[7] Cuffin B N and Cohen D 1977 *IEEE Trans. Biomed. Eng.* **24** 372

[8] Lutkenhoner, Lehnertz B K, Hoke M and Pantev C 1991 *Acta OtoLaryngol* **491** 94

[9] Jerbi K, Mosher J C, Baillet S and Leahy R M 2002 *Phys. Med. Biol.* **47** 523

[10] Koch H and Haberkorn W 2001 *Phil. Trans. R. Soc. Lond.* **359** 1287

[11] Nenonen J, Katila T, Leinio M, Montonen J, Makijarvi M and Siltanen P 1991 *IEEE Trans. Biomed. Eng.* **38** 648

[12] Wang Q, Ma P, Lu H, Tang X Z, Hua N and Tang F K 2009 *Chin. Phys.* B **18** 5566

[13] Hughett P 1995 *Ann. Biomed. Eng.* **23** 506

[14] Wang J Z, Williamson S J and Kaufaman L 1992 *IEEE Trans. Biomed. Eng.* **39** 665

[15] Wang J Z 1993 *IEEE Trans. Biomed. Eng.* **40** 387

[16] Barr R C, Ramsey M and Spach M S 1977 *IEEE Trans. Biomed. Eng.* **24** 1

[17] Fuchs M, Drenckhahn R, Wischmann H A and Wagner M 1998 *IEEE Trans. Biomed. Eng.* **45** 1336

[18] Osama A M and Fuat G U 1993 *IEEE Trans. Magnet.* **29** 1403

[19] Jukka S 1987 *Phys. Med. Biol.* **32** 11

[20] Hamalainen M S and Sarvas J 1989 *IEEE Trans. Biomed. Eng.* **36** 165

[21] Hamalainen M S and Ilmoniemi R J 1994 *Med. Biol. Eng. Comput.* **32** 35

[22] Hansen P C and O'Leary O P 1993 *SIAM J. Sci. Stat. Comput.* **14** 1487

[23] Shou G F, Xia L, Jiang M F, Liu F and Crozier S 2008 *IEEE Trans. Biomed. Eng.* **55** 1327

[24] Horacek B M, Purcell C, Lamothe R, Leon L J and Merritt R 1987 *Phys. Med. Biol.* **32** 121

[25] Purcell C J, Stroink G and Horacek B M 1988 *IEEE Trans. Biomed. Eng.* **35** 671